Deployable Self-Regulating Centrifugally-Stiffened Decelerator (DESCENT): Design Scalability and Low Altitude Drop Test

DOI:
10.1016/j.ast.2021.106710

Document Version
Accepted author manuscript

Deployable Self-Regulating Centrifugally-Stiffened Decelerator (DESCENT): Design Scalability and Low Altitude Drop Test

Rui Wu[a,b,*], Peter C.E. Roberts[b], Lulu Xu[c], Constantinos Soutis[b], Carl Diver[d]

[a] *Laboratory of Robotics and System, Harbin Institute of Technology, P.R.China*
[b] *The University of Manchester Aerospace Research Institute, UK*
[c] *School of Materials, the University of Manchester, UK*
[d] *Department of Engineering, Manchester Metropolitan University, UK*

Abstract

A previous study by the authors has proposed a foldable heat shield that deploys by harnessing the re-entry kinetic energy, namely DEployable, Self-regulating, CENTrifugally-stiffened decelerator (DESCENT). The design benefits from being self-regulating and lightweight, having low requirement on thermal protection, and allowing downrange manoeuvre based on conventional attitude control devices. The present study demonstrates that the system mass can be scaled across 6 orders of magnitude using a set of relatively simple design rules, showing the potential to realise miniaturised entry probes that are simple and robust, with a possible mass-reduction of $> 25\%$ to an 8 m diameter inflatable heat shield. A scaled-down test model with a stitched fabric aeroshell and on-board sensors is drop-tested at low altitude, showing satisfactory agreement with simulation, and no sign of instabilities, paving the way for future higher fidelity tests. The similarity between the low speed drop-test result and Newtonian hypersonic simulation suggests that the critical behaviour of DESCENT is dominated by its geometrical characteristics.

Keywords: Centrifugal deployment, Origami, Heat shield, Entry vehicle, Penetrator probe, Drop test

Nomenclature

F: thrust force (N)

g: Earth gravity (m/s^2)

*Corresponding author
Email address: wurui_hit@hit.edu.cn (Rui Wu)

h: altitude (m)

I_{SP}: specific impulse (s)

l: vehicle characteristic length (m)

m: mass (kg)

M_E: deploying moment due to shell's elasticity (N·m)

N_t: thickness scaling exponent

q: dynamic pressure (Pa)

Q_s: stagnation point heat flux (W/m^2)

r: distance from the rotational axis (m)

R_s: stagnation point radius (m)

S: frontal area (m^2)

ST: Strouhal Number

t: heat shield thickness (m)

v: velocity (m/s)

β: ballistic ratio (kg/m^2)

θ: deployment angle (degree)

ρ: volumetric density (kg/m^3)

τ: roll torque (N·m)

ω: vehicle spin rate (rad/s)

CFRP: Carbon Fibre Reinforced Plastic

CGT: Cold Gas Thruster

DECENT: DEployable, Self-regulating, CENTrifugally-stiffened decelerator

HEART: High-Energy Atmospheric Re-entry Test

IMU: Inertial Measurement Unit

LEO: Low Earth Orbit

MEMS: Micro-Electro-Mechanical Systems

TPS: Thermal Protection System

1. Introduction

Deployable atmospheric entry decelerators and heat shields have attracted increasing interest from space industry during the last decade. Unlike conventional rigid aerodynamic decelerators, deployable heat shields can be stowed compactly during launch, then deploy and achieve low ballistic ratio during entry. The reduced ballistic ratio leads to early deceleration, reduced terminal velocity, and lower aerothermodynamic heating, therefore enables soft-landing of heavy payloads through thin Martian atmosphere [1, 2, 3], as well as flights with extensive heating such as missions to Venus [4, 5]. Meanwhile, a low stowage profile is not only crucial for large entry vehicles to fit inside launcher fairings, but also enables entry systems as small as CubeSats [6, 7, 8, 9, 10].

Current deployable entry systems are mostly based on inflatable structures or foldable mechanisms. Inflatable heat shields use flexible air-tight chambers that are folded before inflation, then deploy and rigidise under internal gas pressure. Flexible thermal protection layers based on commercial materials are wrapped onto the chambers to maintain an acceptable structural temperature [11, 12, 13, 14, 15, 16, 17, 18, 19, 20, 21, 22, 23]. The foldable mechanisms utilise umbrella-like designs where a skirt made of flexible thermal protection materials is bounded onto rigid deployable ribs. Revolute or translational joints allow the ribs to fold and unfold, thereby deploy the skirt and potentially perform flight manoeuvres by manipulating the skirt's shape [24, 25, 26, 27, 28, 29, 30, 31].

A previous study has proposed a new type of deployable heat shield, namely DEployable, Self-regulating, CENTrifugally-stiffened decelerator (DESCENT) [32, 33]. Unlike the current solutions that rely on elastic stabilising forces from either solid or gaseous (i.e. inflation gas) materials, this design concept utilises centrifugal force, which is an inertial force, to deploy and stiffen the heat shield structure. The design benefits from the low structural mass enabled by centrifugal deployment, and realises a less-demanding thermal control scenario. Meanwhile, the deployment is achieved using a self-moderating autorotation during descent. This leads to a fully passive system that automatically deploys and adapts to the varying environment by harnessing the re-entry kinetic energy. The previous study also suggested that the extent of deployment can be actively adjusted using conventional torque-generating attitude control devices, which

moderates the rate of autorotation and thereby enables downrange manoeuvring.

Based on the design studies performed previously [32, 33], the present work demonstrates the scalability of DESCENT, and thereby the possibility to adapt this design to a wide range of aerospace applications. Feasibility of re-entry vehicles with entry mass scaled from 30 g to 30 tonne is discussed based on the entry trajectory and structural dynamic behaviour predicted by simulation. However, the flexible structure of DESCENT makes it challenging to fully understand the high-fidelity aeroelastic behaviour of the heat shield as well as its effect on the entry vehicle's flight dynamics. Therefore, a scaled-down test vehicle is fabricated and drop tested from ∼100 m altitude to reveal its behaviour at low speed and to verify the critical aspects of the simulation.

2. Design scalability of the centrifugally deployed heat shield

2.1. Conceptual entry vehicles with DESCENT

DESCENT uses a uniform flexible shell which buckles into a spiral shape when deformed by aerodynamic load. The buckled shape generates aerodynamic roll-torque during descent in atmosphere, thus induces autorotation. Meanwhile, the centrifugal force caused by the autorotation deploys and flattens the flexible shell. The spin rate then reaches a point that the effect of inertial (centrifugal and axial deceleration) forces on the shell balances the aerodynamic force, while the shell is flattened to an extent that the roll-torque becomes zero. The shell's shape and the spin rate thereby reaches equilibrium. Two conceptual designs of DESCENT entry vehicles are illustrated in Fig. 1 and 2.

Design 1 uses a deployable first stage to minimise the stowed diameter when folded (Fig. 1c). When deploying, the first stage unpacks the shell and facilitates the centrifugal deployment of the flexible second stage [32]. This first stage can be inflatable (for large vehicles) or mechanically deployable structures (for small vehicles), but is not the scope of the present study. The conventional rigid nose cone is installed to protect the payload vessel (an example is given in Fig. 1b). The flexible shell can be made from woven ceramic fabrics such as the test-proven 3M$^{\text{TM}}$Nextel$^{\text{TM}}$based on alumina-boria-silica fibres [34, 35], and a stitched fabric architecture is illustrated by the test model discussed in section 3.2. Packing is demonstrated by a prototype made of latex rubber (Fig. 1c), where the shell folds through an origami pattern with crease lines aligned along the spiral shape.

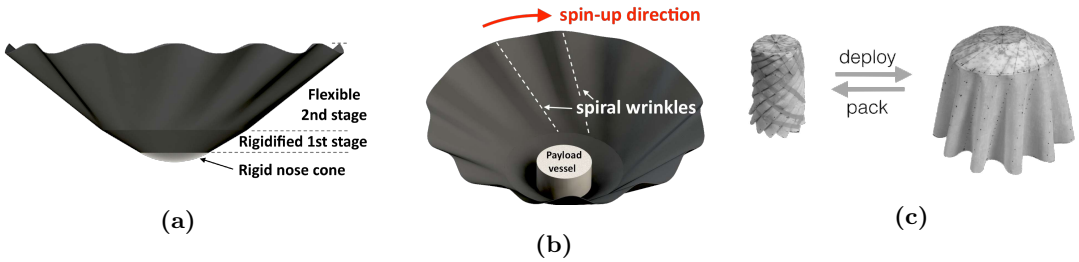

Fig. 1. Design 1 vehicle with centrifugally deployed heat shield, (a) side view showing the basic components of a vehicle with two-stages deployment, (b) tilted view showing the payload vessel, (c) packing of the heat shield demonstrated by a latex rubber prototype, which folds along an origami crease pattern.

Design 2 (Fig. 2a) has removed the first stage for simplicity, and replaced it with a larger nose cone. For a miniaturised vehicle, a symmetrical payload vessel can be used to realise a robust design that guarantees thermal protection even if the vehicle tumbled and flipped over before entry: an example is given in Fig. 2b, where two identical nose cones are oppositely closed up to provide a payload space in between. When flipped, the payload is still protected by the nose cone that was on the aft side before flipping, while the flexible shell snaps through into the correct conical shape under aerodynamic load. Such a design guarantees data recovery after test flights, and also enables miniaturised swarm-probes without pre-spin or active attitude control.

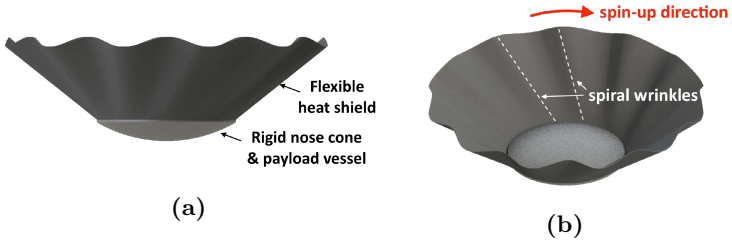

Fig. 2. Design 2 vehicle with a simplified centrifugally deployed heat shield, (a) side view with single-stage deployment and enlarged nose cone, (b) tilted view showing the symmetrical cargo bay that allows reversed flight to relieve the requirement for attitude control or pre-spin.

2.2. Scaling of a fully passive DESCENT system

Previous study has demonstrated that a CubeSat sized vehicle can reach near full deployment (forming a blunt cone) throughout the hypersonic and supersonic flight regimes during a re-entry from Low Earth Orbit (LEO) [32], and a downrange manoeuvrability of order 10^2 km is achievable using a commercial reaction wheel [33]. In this section, it is shown that the design can be scaled-up while achieving similar performance using three simple scaling rules:

1) Entry mass follows volumetric scaling, where l is the vehicle's characteristic dimension:

$$m_{vehicle} \propto l^3 \tag{1}$$

2) Heat shield material density is independent of scaling, while its thickness scales as:

$$t \propto l^{0.7} \tag{2}$$

3) Heat shield maintains geometric similarity during scaling.

During scaling, the Strouhal Number ST stays constant due to the similarity of geometry (when Reynolds number and Mach number effects are ignored):

$$ST = \frac{\omega \cdot l}{v} \tag{3}$$

In other words, the flow structure scales together with the shell while maintaining geometric similarity. This can be further explained below: The aerodynamic roll torque is predicted by integrating the Newtonian aerodynamic pressure on an origami-shaped geometrical model [32]. In the rotating shell's reference frame, at a distance of r from the rotational axis, the angle between local freestream and the rotational axis is given by $\arctan(\omega r/v)$, where ω is the rate of rotation, and v is the freestream velocity. Since Reynolds number and Mach number effects are ignored, the aerodynamic roll-torque acting on the shell purely depends on the local angles of attack, thus depends on the local freestream direction and the shell geometry. With the shell maintaining geometric similarity, the roll-torque purely depends on $\arctan(\omega r/v)$. Therefore, the Strouhal Number $\omega l/v$ at equilibrium (when roll-torque is zero) is independent of scaling

(note that $r \propto l$ due to similarity).

The deployment dynamics of the shell is predicted using Newtons laws. Since the shape undulation has minor structural dynamic effect, the simplified geometrical model ignores the wrinkles, thus the whole shell is considered to have a unique deployment angle at any time. The inertial and Newtonian aerodynamic forces are then evaluated across the shell to simulate deployment. The deploy-ability of the shell can be derived using Eq. 4 (Eq. 14 in [32]), where ω is the rate of autorotation, q is dynamic pressure, θ is deployment angle (instantaneous semi-vertex angle of the shell, with full deployment set to 60°), and ρ_{shell} is the shell material's density:

$$\omega \propto \sqrt{\frac{q \cdot \tan(\theta)}{l \cdot \rho_{shell} \cdot t}} \tag{4}$$

Simplify by specifying constant Strouhal Number, we have:

$$\tan(\theta) \propto \frac{\rho_{shell} \cdot t}{\rho_{air} \cdot l} \tag{5}$$

The scaling of thickness is determined by $t \propto l^{N_t}$, where N_t is the thickness scaling exponent. Eq. 5 suggests that the deployment angle can be independent of scaling if $N_t = 1$, which is thereby a natural scaling strategy from a structural dynamics point of view. However, $t \propto l$ gives unnecessarily thick heat shield when the design is scaled up, thus the ideal scaling strategy should have $N_t < 1$ to prevent excessive heat shield thickness variation while maintaining acceptable structural dynamic performance. In this preliminary study, $t \propto l^{0.7}$ (Eq. 2) is used. As a result, the heat shield mass satisfies $m_{shell} \propto l^{2.7}$, thus a scaled-up vehicle will have a lower heat shield mass fraction ($m_{shell}/m_{vehicle} \propto l^{-0.3}$). Despite this reduced mass fraction, when scaled up the heat shield still provides more than sufficient thermal protection as discussed in Section 2.4, which suggests that an even lower N_t could be practical. Meanwhile, substituting Eq. 2 into Eq. 5, we have Eq. 6, which suggests that the deployment angle under a certain altitude (or air density, ρ_{air}) tends to be slightly lower when the vehicle is scaled up:

$$\tan(\theta) \propto \frac{\rho_{shell}}{\rho_{air} \cdot l^{0.3}} \tag{6}$$

Numerical simulations are carried out to predict the autorotation and deployment of scaled

vehicles throughout re-entry from LEO. The simulations are conducted by coupling a trajectory simulator with a structural dynamic model and a autorotation aerodynamic model. The trajectory simulator utilises Newton's laws of motion and Newtonian hypersonic aerodynamics to numerically simulate the 3D trajectory of a point-mass ballistic entry vehicle. The simulator considers the three translational degrees of freedom along the three Cartesian axes, and the equations of motion are formulated using Newton's second law. Exponential atmospheric model is used: $\rho_{air} = \rho_0 \, e^{-h/H}$, where h is altitude, ρ_0 and H have values of 1.752 kg/m^3 and 6700 m, respectively. The structural dynamics as well as the hypersonic autorotation behaviour are predicted using analytical equations derived from a simplified geometrical model. The model assumes the shell always has axisymmetrical deployment and zero angle of attack [32]. Stagnation point aerothermodynamic heating Q_s is predicted using the Sutton and Graves equation shown below, where R_s is the radius of stagnation point. This equation accounts for the convective heat transfer through a non-reacting laminar boundary layer [36, 37].

$$Q_s = 1.83 \times 10^{-4} v^3 \sqrt{\frac{\rho}{R_s}} \tag{7}$$

The simulation includes seven design examples covering vehicle masses ranging across six orders of magnitude, and assumes Earth re-entry from 145 km altitude at 7.8 km/s and zero flight path angle. Very low vehicle masses (30 g and 300 g) are included as they may allow new types of exploration missions with a swarm of small probes, including atmospheric probes and planetary penetrators [38]. It can be seen that scaling the vehicle barely influences the peak deceleration and stagnation point heating (Fig. 3 and Table 1). Heat flux usually increases with ballistic ratio, but such effect is cancelled out by the variation of stagnation point radius (Eq. 7). Meanwhile, the average deployment angle decreases with increasing vehicle size as predicted by Eq. 6. For the same reason, a larger heat shield can reach a lower instantaneous deployment angle, leading to a higher aeroelastic oscillation (i.e. oscillation in deployment angle, which is investigated in the previous study [33]), which in turn increases the fluctuation in deceleration. However, it should be said that in reality such oscillation will be reduced by the damping effect from the flexible heat shield material, as well as the aerodynamic damping effect that opposes the flapping (local structural motion associated with the deploying-folding oscillation) of the

heat shield. The simulation reported here has not included structural or aerodynamic damping since the focus is on the baseline structural dynamic behaviour.

In addition, since ballistic ratio increases with vehicle size: $\beta \propto l$ (derived from Eq. 1), the peak dynamic pressure also increases, according to Table 1, it follows the relation derived by H. Julian Allen [39]: $q \propto l$. Therefore the scaling of spin rate (Eq. 4) becomes $\omega \propto l^{-0.35}$. The fact that a larger heat shield tends to have a lower spin rate is beneficial since it limits the tensile stress in the flexible structure. However, the exact stress cannot be evaluated without a detailed heat shield design, thus is not further discussed.

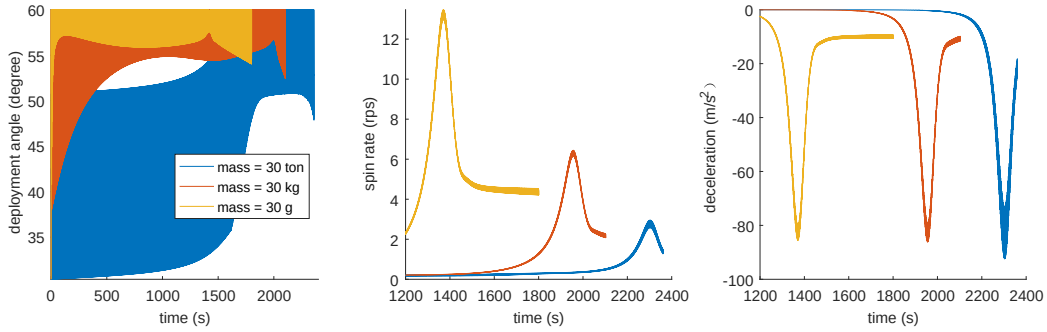

Fig. 3. Scaled vehicle with entry mass of 30 g, 30 kg and 30 tonne, simulated for re-entry from 145 km LEO with zero flight path angle, descending to 30 km altitude, illustrating the effects of scaling-up: lower deployment angle, lower spin rate, similar peak deceleration, and higher oscillation in the absence of damping.

Table 1: Vehicle setup and numerical simulation results corresponding to the scalability study in Fig. 3.

Vehicle mass	Max. diameter	Ballistic ratio[b]	H.S. surface density	H.S. mass fraction	Peak spin rate	Peak P	Peak deceleration	Peak heating[c]
30 g	0.15 m	1.1 kg/m^2	0.37 kg/m^2	25%	13 rps	87 Pa	8.4±0.3 G	25.4 W/cm^2
300 g	0.32 m	2.4 kg/m^2	0.66 kg/m^2	20%	10 rps	190 Pa	8.4±0.3 G	25.3 W/cm^2
3 kg	0.7 m	5.2 kg/m^2	1.1 kg/m^2	16%	8.1 rps	400 Pa	8.4±0.3 G	25.4 W/cm^2
30 kg	1.5 m	11 kg/m^2	1.9 kg/m^2	13%	6.3 rps	870 Pa	8.4±0.4 G	25.6 W/cm^2
300 kg	3.2 m	24 kg/m^2	3.2 kg/m^2	9.9%	4.8 rps	1.9 kPa	8.4±0.5 G	25.5 W/cm^2
3 tonne	7 m	52 kg/m^2	5.5 kg/m^2	7.9%	3.7 rps	4.2 kPa	8.4±0.6 G	25.8 W/cm^2
30 tonne	15 m	112 kg/m^2	9.5 kg/m^2	6.3%	2.8 rps	9.3 kPa	8.5±0.9 G	26.2 W/cm^2

[a] H.S.: Heat Shield
[b] Ballistic ratio at full deployment
[c] Stagnation point convective heating

2.3. Scaling of a DESCENT system with actively adjusted deployment

Besides the basic behaviour discussed above, the downrange manoeuvrability can also be scaled up. Previous study has predicted an open-loop downrange manoeuvrability of over 300 km during simulated re-entry of a CubeSat-sized vehicle, as well as a method to suppress the aeroelastic oscillation [33]. This was achieved using an off-the-shelf reaction wheel coordinated by a switching gain-scheduled controller, which actively adjusts the spin rate of a CubeSat-sized vehicle, and thereby influences the deployment angle and drag coefficient. Here a scalable system is designed with actively controlled Cold Gas Thrusters (CGTs), which is more straightforward to scale than reaction wheels used in the previous study [40]. The CGTs operate continuously while the thrust is controlled at 40 Hz. Since the baseline behaviour of scaled systems is of interest, the thrust response is assumed to be instantaneous and no noise is included in the controller. The thrusters are tangentially installed at the edge of the design 1 payload vessel (the design with 3 kg mass is based on a CubeSat architecture, for which we assume a moment arm of 6 cm, and scales linearly with l) to generate a roll-torque, τ_{CGT}.

On the other hand, the aerodynamic roll-torque generated from the spiral shell geometry satisfies the expression below (note that $q \propto l$ as discussed earlier):

$$\tau_{aero.} \propto q \cdot S \cdot l \propto l^4 \tag{8}$$

The total roll-torque $\tau_{aero.}+\tau_{CGT}$ then determines the spin rate and thereby the deployment. The similitude of control therefore requires $\tau_{CGT} \propto \tau_{aero.}$, which means the control similitude factor can be defined as:

$$\frac{\tau_{CGT}}{l^4} \tag{9}$$

Since $\tau_{CGT} \propto F_{CGT} \cdot l$, we have $F_{CGT} \propto l^3$. Assuming Nitrogen-propellant CGTs with a specific impulse of 70 s, the propellant consumption rate can be evaluated using the equation below [41]:

$$F_{CGT} = g \cdot I_{SP} \cdot \dot{m} \tag{10}$$

Where g is Earth's gravity, I_{SP} is specific impulse, and $\dot{m}$ is fuel mass flow rate. The

controller developed in the previous study is then scaled and simulated with two vehicle sizes. The results are shown in Fig. 4 and Table 2. Note that the control similitude factor of 0.04 is chosen here as it provides satisfactory control authority with acceptable propellant consumption rate. For simplicity, the vehicle mass variation due to propellant consumption is not considered in the simulations.

The simulation reported in this section starts from 125 km rather than 145 km altitude (as in the last section) because: oscillation suppression is not necessary at very high altitude, as the damping effect from heat shield material will be sufficient to stabilise the weak aeroelastic oscillation in a thin atmosphere; due to the thin atmosphere, downrange manoeuvre at high altitude is less effective in terms of propellant consumption, therefore the controller is assumed to be activated at a lower altitude. Nevertheless, it is possible to use a different control algorithm in the upper atmosphere to enable earlier downrange manoeuvre without excessive propellant consumption, while the emphasis here is on the more demanding flight regime in the denser atmosphere. Simulation results are shown in Fig. 4, where the oscillation in deployment angle is suppressed, removing the fluctuation in deceleration (comparing with Fig. 3). Meanwhile, downrange shifts of $\sim$ 540 km are achieved for both vehicle sizes with propellant consumption below 7% of vehicle mass (for reference, the NASA Mars Science Laboratory is fuelled by hydrazine that makes approximately 10% of the entry mass [42]).

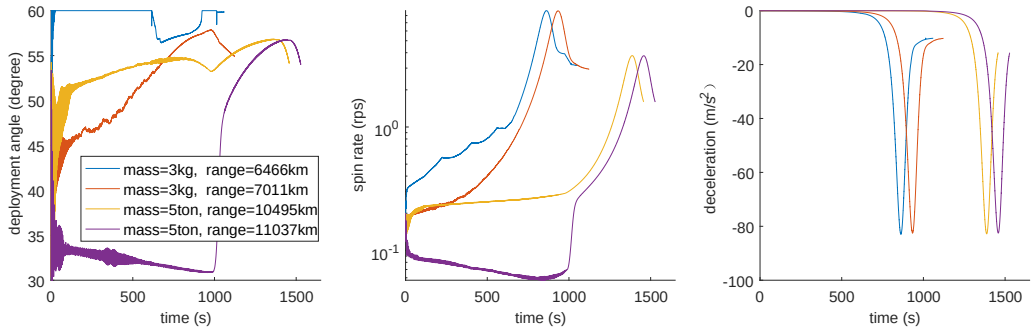

Fig. 4. Scaling of a vehicle with total mass of 3 kg and 5 tonne, and actively controlled CGTs with similitude factor $\tau_{CGT}/l^4 = 0.04$ to adjust downrange, simulated for re-entry from 125 km LEO with zero flight path angle, descending to 30 km altitude, showing that a $\sim$ 540 km downrange manoeuvrability can be achieved while suppressing aeroelastic oscillation.

Table 2: Vehicle setup (design 1) and simulation results corresponding to the scalability study in Fig. 4, with control similitude factor $\tau_{CGT}/l^4 = 0.04$.

Vehicle mass	τ_{CGT}	Total downrange shift	Propell. consumption	Propell./Vehicle mass	Downrange goal
3 kg	$0.0094\ N \cdot m$	545 km	0.11 kg 0.18 kg	4% 6%	Reduce Increase
5 tonne	$186\ N \cdot m$	542 km	200 kg 357 kg	4% 7%	Reduce Increase

2.4. Case study: comparison with an inflatable entry decelerator

The 5 tonne vehicle scaled in this study has a maximum diameter of 8.3 m. This is similar to NASA's High-Energy Atmospheric Re-entry Test (HEART) vehicle, which is a ballistic entry vehicle concept with an inflatable blunt-cone heat shield designed for space station cargo exchange as well as other planetary entry missions [35]. The key design parameters and entry environments are compared in Table 3. The heat shield mass fraction of HEART is approximated by summarising the mass of the inflatable structure made of silicone-coated Kevlar torus, the Thermal Protection System (TPS) made of layers of fabrics and blankets, and the inflation subsystem consisted of pressure vessel, valves, etc. (while excluding rigid structures and nose cone) [35]. Mass fraction of the present design is evaluated using the mass of the flexible shell (note that design 1 has higher shell mass since it contains a first stage), which serves as the deployable structure and the TPS at the same time. Meanwhile, the stowed diameters reported in the table are based on the size of rigid nose cones (for DESCENT) as well as literature (for HEART) [35].

According to Table 3, DESCENT have shown the potential to be more mass-efficient than HEART. It is worth noticing that the TPS on HEART has two 3M$^{\text{TM}}$Nextel$^{\text{TM}}$440 BF-20 alumina-boria-silica fabrics as the outer-most thermal resisting layer, which is proven to withstand the flight temperature and provides structural integrity during folding, handling and flight. Five layers of insulating blankets and a gas barrier are stitched onto the outer layer's aft side to protect the silicone-coated inflatable torus [35]. In contrast, DESCENT is deployed and stiffened by inertial (centrifugal) force thus mostly relies on the mass rather than the elastic response from heat shield materials, thus is fundamentally convenient for thermal protection. It can potentially be made solely from high temperature fabrics, and no insulation blankets or gas barriers are needed. The heat shield surface density is 6.2 kg/m^2 according to the scaling

rule (Eq. 2), which can be achieved with 12 layers of Nextel^{TM}440 BF-20 fabric. This provides excessive thermal protection compared to the 2 layers on HEART (note that they have similar entry environment as shown in Table 3). It is worth noting that the absence of insulating layers in the TPS leads to a higher heat shield aft surface temperature, which has two consequences: backshell of the payload vessel requires extra insulation to thermal radiation; heat shield front surface temperature decreases due to the extra radiative cooling, which has been briefly discussed previously [32].

Table 3: Comparison between DESCENT and NASA's HEART inflatable system.

Vehicle	Entry mass	Max. dia.	Stowed dia.	H.S. mass fraction	Peak P	Peak decel.	Peak heating[a]
DESCENT	5 tonne	8.3 m	1.5 m (design 1) 3.3 m (design 2)	7.5% (design 1) 6.5% (design 2)	5.8 kPa	8 g	28 W/cm^2
NASA HEART[35]	5 tonne	8.3m	$\sim$ 2.3 m	10%	5.5 kPa	7 g	27 W/cm^2

[a] Stagnation point convective heating

Therefore, the design of DESCENT can potentially be applied to entry systems at a wide range of sizes, with possible mass-reduction over existing inflatable systems. This also indicates that the behaviour of a small test vehicle can be representative for larger systems.

3. Low-speed low-altitude drop test

In the last section, the scalability of DESCENT is discussed based on simulation results. However, it is challenging to fully predict the aeroelastic behaviour of the flexible DESCENT structure, as well as its effect on the entry vehicle's flight dynamics. Therefore, a low speed low altitude drop test is carried out using a scaled-down test vehicle.

Experiments starting in the upper atmosphere at a hypersonic speed is ideal but costly, thus the present work focuses on experimenting under a low-speed low-altitude condition. Such a test certainly cannot capture all the interested aspects including the transonic behaviour and aerothermodynamic heating, but will still provide useful insights and increase the confidence of successfully conducting a higher fidelity test (i.e. orbital/suborbital launch).

Recent tests of NASA ADEPT deployable heat shield have encountered problematic subsonic behaviour associated with an attitude motion coupling at high roll rates, the cause of which is currently unknown to our knowledge [6]. DESCENT has a baseline geometry similar to ADEPT, but with structural compliance and a self-moderated roll rate that is significantly higher than

ADEPT. The flight dynamic behaviour is thereby of great interest. Although the present study is primarily focused on the baseline deployment dynamics, the drop tests have provided insights into the flight dynamic behaviour.

In this section, a scaled-down test vehicle is constructed to demonstrate the flight dynamics during a free-fall drop test from $\sim$ 100 m height, and to verify key aspects of the simulation.

3.1. Information about the simulation

The simulator used here is similar to section 2, besides that the aerodynamic damping and the elasticity of the shell are accounted for. It predicts the coupled autorotation and deployment motion throughout the descent.

To validate the comparability between the simulation and the low-speed drop test results, the difference between the low-speed and hypersonic autorotation aerodynamic behaviour needs to be verified. Therefore, a series of low-speed wind tunnel tests are carried out. As shown in Fig. 5, a scaled-down paper origami model is attached to a jig which allows free rolling of the model through an axle supported by ball bearings, and a tachometer with a code disk is used to measure the roll rate. A disk located along the axle is used to restrict the paper origami from folding under aerodynamic load, which thereby set the deployment angle for testing. For each deployment angle (35°,40°,45°,50°, and 57°, which is the average deployment angle associated with the mountain and valley folds), the test is carried out at freestream velocities of 14 m/s, 16 m/s and 18 m/s, and Strouhal Number (Eq. 3) is evaluated. Strouhal Number obtained with the different freestream velocities has negligible difference, thus the average is reported.

Since the tests are done by free spinning, the measured spin rates are the equilibrium spin rates at which zero aerodynamic roll-torque (or a small roll-torque in equilibrium with the rotational friction from the test jig) is generated. In Fig. 6, the wind tunnel results are plotted over analytical aerodynamic roll-torque, showing a rough agreement. Such an agreement between low speed and hypersonic results indicate that the autorotation of the origami model is dominated by geometric principles whilst the Mach number effect is of secondary importance (which is a natural consequence of spiral-shape initiated autorotation). It also suggests that a low-speed low-altitude drop test could generate meaningful results since the important spinning motion can be replicated at low speed. It should be noted that such a drop test is necessary in order

to reveal the deployment's dynamic behaviour since the effect of lateral gravity in a horizontal wind tunnel causes undesirable distortion when a flexible test model is used.

Fig. 5. The wind tunnel setup, with a paper origami model mounted on a free-spinning axle that spins with a code disk used for spin rate measurement.

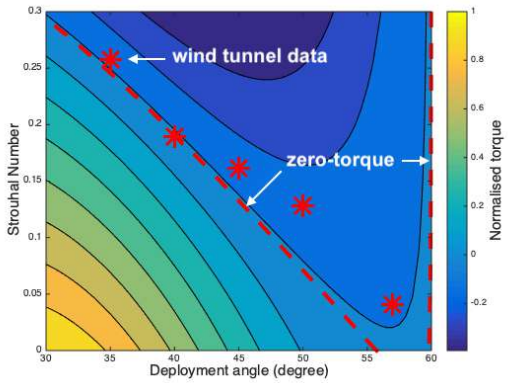

Fig. 6. Aerodynamic roll-torque, where low-speed wind tunnel results are plotted over the analytical results based on Newtonian hypersonic aerodynamics, showing rough agreement.

Meanwhile, aerodynamic damping on the deployment of the flexible heat shield is added into the simulation since it has notable effect at low speed. This is achieved by rewriting the dynamic pressure term used to predict deployment behaviour, in order to account for the local velocity variation caused by the shell's deploying motion:

$$v_{local} = v_{freestream} + l_{shell} \cdot \dot{\theta}/2 \tag{11}$$

Where $\dot{\theta}$ is the angular velocity of the shell's deploying motion, l_{shell} is the length of the flexible shell on a cross section through the rotational axis. The effect of the shell's elasticity is also accounted to improve the fidelity of the model: The elastic effect tends to let the shell recover

to a neutral deployment angle, which is assumed to be 50°. It is not set to the full deployment angle of 60° since the neutral shape of the fabric shell (section 3.2) is not flat considering the effect of repeated folding and stitching. According to the experimental observation that under $-1\ g$ environment the deployment angle is 28.5° rather than zero due to the effect of elasticity, the elastic deploying moment at 28.5° can be evaluated. Then the elastic deploying moment $M_E(\theta)$ at any deployment angle is estimated by assuming a linear relation. The elastic deploying moment can have an effect, but this is not a dominating factor at low altitude:

$$M_E(\theta) = \frac{50 - \theta}{50 - 28.5} \cdot M_E(28.5^\circ) \tag{12}$$

3.2. Test model construction

The drop test model is based on design 2 (Fig. 2), and has a maximum diameter of 0.7 m, a semi-vertex angle of 60°, the nose cone has a diameter of 0.3 m, and a curvature radius of 0.15 m. The mass of the model when tested is 610 g, in which the shell contributes 290 g. The flexible shell is fabricated using a heavy duty fabric with high resistance to in-plane shear. The fabric is tailored into twelve identical elements shown in Fig. 7, and stitched together along the edges by creating double lap seams with top-stitch (note that the gap on the upper left of the origami pattern is closed to form the conical shell). Such a seam structure has high strength and creates a pocket that can be used to enclose structural members for local reinforcement [43]. In the drop test model, local reinforcements made of Carbon Fibre Reinforced Plastic (CFRP) strips are inserted to induce structural anisotropy and therefore inducing a predictable spiral shape when the shell folds by buckling (Fig. 8a). The CFRP strips are lightweight (approx. 3 g each) thus has negligible effects on the deployment behaviour. This stitched fabric architecture is similar to NASA's ADEPT concept [44].

The drop test system is illustrated in Fig. 9. The test vehicle suspends below the hanger through releasing mechanisms that are manually controlled using a remote controller. Floating of the balloon is manually controlled from ground using a continuous cable passing through pulleys.

3.3. On-board sensors & data processing

All measurements are made on board the test vehicle using a video camera with fisheye lens, and a commercial UAV flight controller (Pixhawk) with a MEMS (Micro-Electro-Mechanical

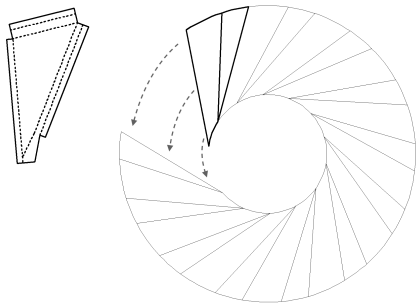

Fig. 7. The origami pattern (right) upon which the shell is designed, and the fabric element for the test vehicle (left) with dashed folding lines, note that the gap on the upper left needs to be closed to form the conical shell.

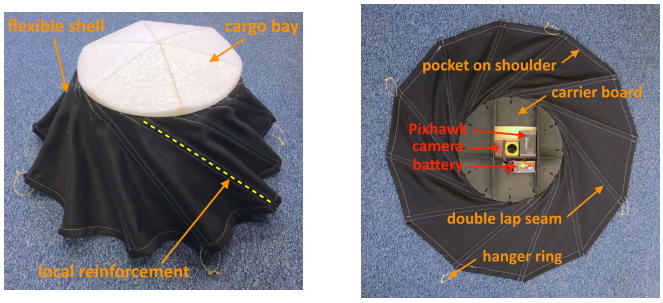

(a) **(b)**

Fig. 8. The test vehicle, (a) side view, showing the spiral shape that simultaneously forms when the shell folds by buckling, (b) top view showing the carrier board on the cargo bay.

Systems) IMU (Inertial Measurement Unit), a MEMS barometer, and a micro-SD card for data-logging. The function of these sensors are listed in Table 4.

Velocity, which is mainly vertical, is evaluated based on the altitude information from the barometer. The spin rate is measured using the gyroscope. The vehicle attitude is recorded by the IMU, which fuses the measurement from various sensors using an extended Kalman filter and outputs the three Euler angles (roll, pitch and yaw). All the measurements made by the Pixhawk have a sample rate of 10 Hz. The deployment angle is retrieved from the images captured by the upward facing camera. The images are converted from a video taken at 60 frames per second and the resolution of 1280×960 pixels. The lens has a 220° view angle and equidistant projection after image calibration.

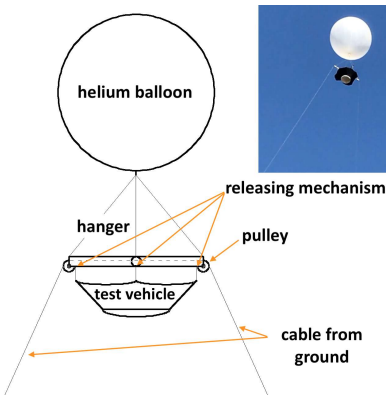

Fig. 9. The drop test system consisted of a lifting helium balloon, a hanger controlled from ground, and test vehicle suspending under the hanger through remote-controlled releasing mechanisms.

Table 4: Measurements from the sensors on board the test vehicle.

Measurement	Sensor	Specification
Velocity (altitude)	Barometer	MS5611 IMU
Spin rate	Gyroscope in IMU	MS5611, allowing up to $2000°/s$
Attitude	IMU	MS5611, with Kalman filter
Deployment angle	Upward facing camera	Fisheye lens with equidistant projection, 1280×960 pixels

Deployment angle is measured by an image processing program, which separates the flexible shell from the background and distinguishes the edges of the shell. Fig. 10 shows a typical image taken during the drop test. It can be seen that only the centre of the image is within the projection area of the lens and the corners are dark. The vehicle and the flexible shell are also dark except the white yarns used to stitch the shell together. The rest of the image is mostly blue sky that is relatively bright especially in the blue colour channel. Therefore, a threshold is applied to binarise the image by setting all the pixels with $< 60\%$ brightness in the blue channel to black and the rest to white. This is followed by a series of process that eliminate the lens flare while minimising artifacts (Fig. 10).

The processed image is then used to evaluate deployment angle. Every pixel on the edge of the shell is treated as an equal section of the edge, and the deployment angle of such a section can be solved from the view angle using simple geometry. The images are calibrated using a mapping function provided by the lens supplier before the evaluation of deployment angle.

The sensitivity to binary threshold is analysed by trails to guarantee reliable deployment angle measurement.

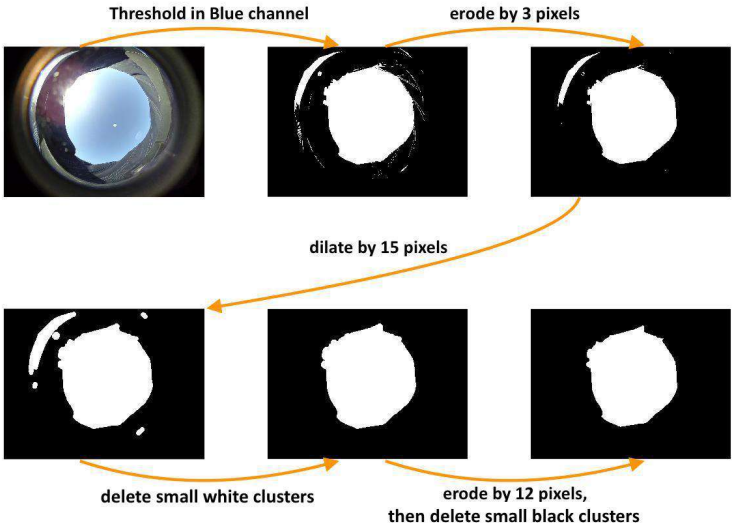

Fig. 10. Image processing used to pick up the shell's edge from images taken by on-board camera, showing the lens flare removed from the final image.

3.4. Results & Discussion

Three drop tests are conducted. Fig. 11 shows the distribution of deployment angles corresponding to all the edge pixels on 40 processed frames taken during 8 s $\sim$ 12 s of the descent. As the flexible shell in real world is not axisymmetric and always contains wrinkles and defects, the edge pixels have a range of deployment angles rather than a single value as assumed by the simulation. However, a distinct peak at approx. $50° \sim 53°$ exists in the data from all the three test runs, which means most part of the edge has similar deployment angle, thus the shape of the shell is regular and predictable. Then the average deployment angles corresponding to all edge pixels in each frame is defined as the overall deployment angle at that frame.

In Fig. 12, the drop test results are plotted in comparison with simulation results, where the zero altitude is set as the releasing altitude. It can be seen that the terminal velocity is achieved at approximately 2 s into the descent, reaching a Reynolds number of $Re/m = 4 \times 10^5$ whilst the Mach number is close to zero. The descent predicted by simulation has satisfactory agreement with the tests. The spin rate and deployment angle shown in Fig. 12b and Fig.

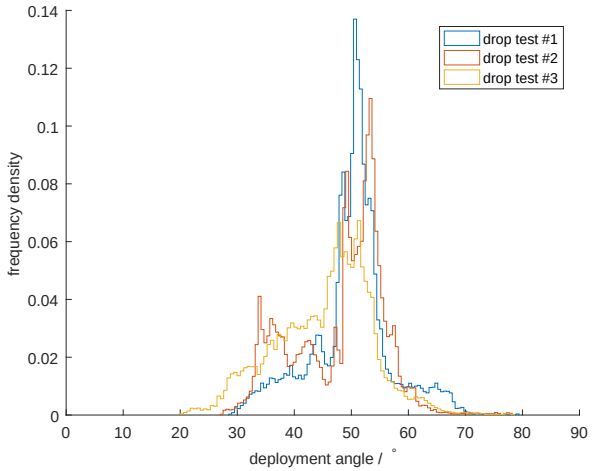

Fig. 11. Distribution of deployment angles corresponding to all the edge pixels on 40 processed frames taken during 8 $\sim$ 12 s of descent, note that most part of the shell has deployment angle of 50° $\sim$ 53°, suggesting a shell geometry that is regular and predictable.

12c have close agreement with simulation except at the beginning of descent, where the initial spin-up and deployment is not as rapid as predicted by the simulation.

According to this result, the simulation is making reasonable prediction of the equilibrium spin rate, as well as the deployment of the aeroshell under inertial and aerodynamic load, though the speed of the initial deployment is over-predicted.

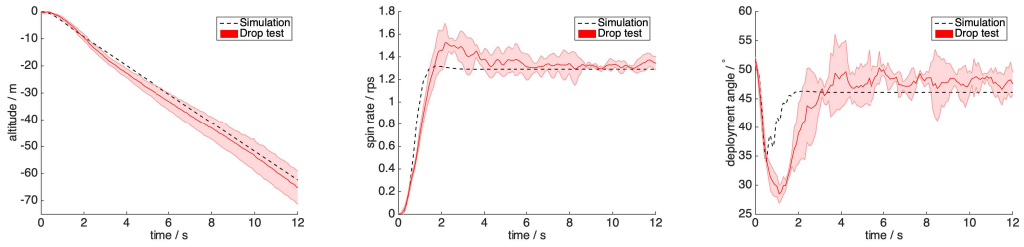

(a) **(b)** **(c)**

Fig. 12. Drop test results plotted in comparison with simulation, where the error band represents one standard deviation, (a) altitude, with zero point set as the releasing altitude of the test vehicle, showing satisfactory agreement, (b)(c) spin rate and deployment angle, showing close agreement except at the beginning of the drop, suggesting that the simulation has reasonable prediction of equilibrium condition, though it reaches equilibrium more rapidly.

Besides validating the key simulation parameters (i.e. spin rate and deployment angle), the flight dynamics of the vehicle is also of interest. It is worth noticing that the peak of the deployment angle distribution as shown in Fig. 11 is between 49° and 53°, which is different from the equilibrium overall deployment angle of approx. 48° as shown in Fig. 12c. This is due to the fact that at such a low overall deployment angle, the shell buckles into an unsymmetrical mode as it folds. It can be seen from Fig. 13 (and video clips in supplementary materials S1) that from before 3 s into the descent, this mode starts to cause the fabric elements on the lower left side of the shell in the image to fold up extensively, leaving the rest elements relatively flat. The relatively flat elements thereby have deployment angles of between 49° and 53°, and the extensively folded elements have a lower deployment angle (34° $\sim$ 48° according to Fig. 11), while the average deployment angle generally satisfies the simulation prediction based on the axisymmetric geometrical model.

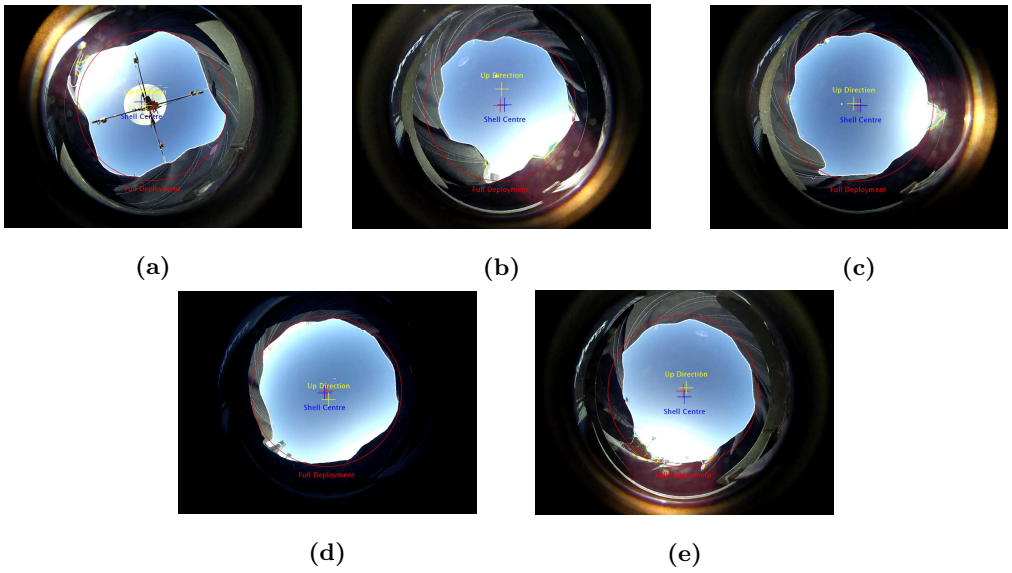

Fig. 13. Images from the upward facing camera taken at (a) 0 s, (b) 3 s, note that an unsymmetrical shape is formed due to the low deployment angle, which causes the fabric elements on the lower left to fold extensively, such buckling mode persists to the end of the descent, (c) 6 s, (d) 9 s, (e) 12 s; converted from supplementary material S1.

The unsymmetrical shape of the aeroshell discussed above also leads to a non-zero angle of attack of the vehicle. Fig. 14 shows the vehicle attitude dynamics history, where the nadir angle,

which is the angle between the Earth gravity vector and the vehicle attitude (downward facing vector bonded to the vehicle) is plotted. According to this figure, the vehicle has a non-zero nadir angle that decays during the descent, while the motion contains autorotation and nutation (coneing motion).

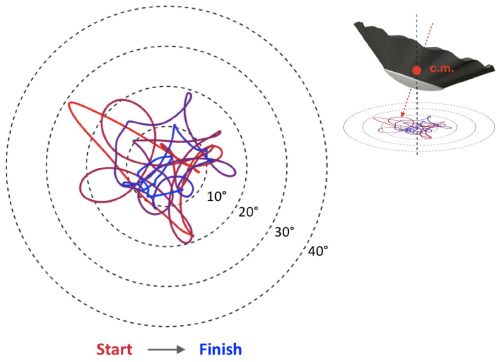

Fig. 14. Vehicle attitude dynamics history during the first drop test, plotted using the pitch angle and pitch direction in the inertial frame, with colour representing descending time, the motion caused by autorotation and nutation can be seen from this plot.

The nutation motion is illustrated with better clearance in Fig. 15, where the vehicle's yaw angle is set to zero (i.e. plotting the nadir angle in the vehicle frame). It can be seen from Fig. 15a-15c, as well as Fig. 16 that the nutation angle is reducing during the descent. The frequency of the nutation motion evaluated from Fig. 16 is approx. 1.9 Hz, which is different from the rate of autorotation (1.4 Hz according to Fig. 12b).

The unsymmetrical shape is more likely to occur when the system is scaled down and at lower deployment angle, according to the principle of elastic buckling. The effect of asymmetry of a flexible decelerator at high altitude and speed is currently unknown, which is therefore a limitation to scaling the design down to very small sizes. Nevertheless, the system is naturally prevented from reaching a low deployment angle at high altitude (as demonstrated by Eq. 6), thus a very small sized DESCENT entry system is potentially feasible with an elastically-assisted shell that automatically springs to a high initial deployment at the time of entry.

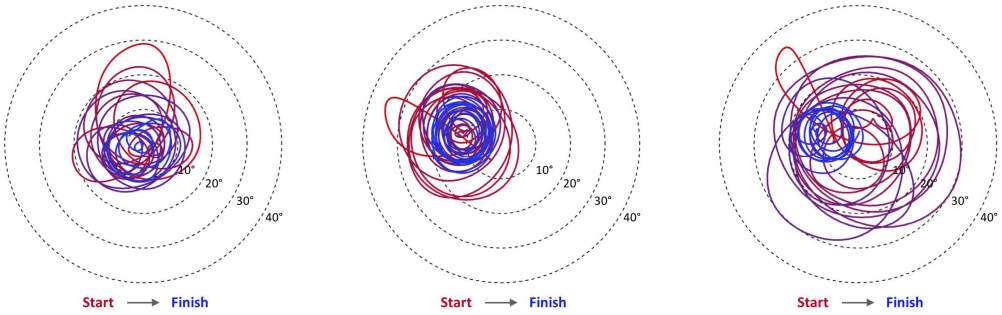

Fig. 15. Vehicle attitude dynamics history of drop tests 1∼3, (a) (b) (c) nadir angle plotted in the vehicle frame with colour representing descending time, the decaying nutation motion is clearly shown by these plots.

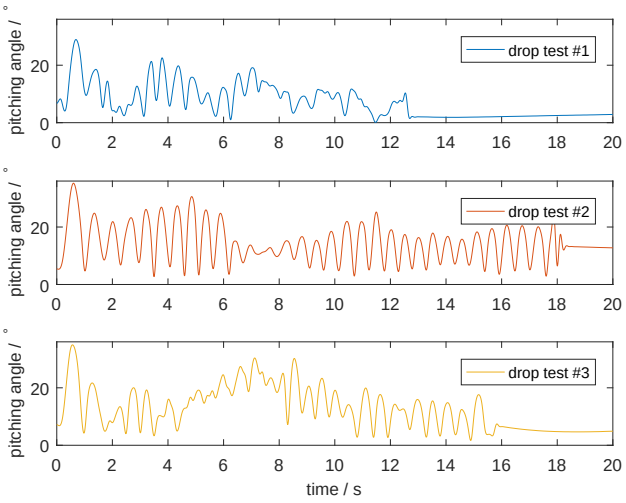

Fig. 16. Vehicle attitude dynamics history of test runs 1∼3, where the nadir angle is plotted against time, showing a nutation frequency (1.9 Hz) that is different from autorotation (1.4 Hz).

4. Conclusions

Scalability of the DEployable, Self-regulating, CENTrifugally-stiffened decelerator (DESCENT) is demonstrated in this study. Following three simple scaling rules, vehicles with entry mass ranging across six orders of magnitude (from 30 g to 30 tonne) have achieved acceptable trajectory behaviour during simulated re-entries from Low Earth Orbit (LEO). The design also shows

a lower heat shield mass fraction when scaled to compare with NASA's HEART inflatable entry vehicle. Downrange manoeuvre enabled by a roll-attitude controller proposed in [33] is also scalable: vehicles with 3 kg and 5 tonne entry mass have achieved similar downrange shift ($\sim$ 540 km) and propellant consumption ($< 7\%$ of vehicle mass) in simulated LEO re-entries.

Two design variations of DESCENT are proposed. In order to address different mission requirements, the designs feature low stowage volume and structural simplicity, respectively. Particularly, the design 2 allows a miniaturised vehicle to survive entry even when flipped over, thus relieving the requirement for attitude control or pre-spin. This potentially provides an entry vehicle solution for miniaturised swarm-probes. The stitched fabric heat shield construction based on such a design is demonstrated by the drop-test vehicle.

According to low speed wind tunnel tests, the simulator, although developed using hypersonic aerodynamics, can predict equilibrium autorotation at low speed. Therefore, the critical aspects of the simulation can be verified by comparing to the low-speed ($\sim$ 5 m/s) low-altitude ($\sim$ 100 m) drop tests conducted in the present research. The simulation shows close agreement to the tests in equilibrium spin rate and deployment angle. Such a similarity between hypersonic and low speed results indicates that the critical behaviour of DESCENT, including autorotation and deployment are dominated by its geometrical characteristics.

Furthermore, during the drop tests the aeroshell folded through an unsymmetrical buckling, leading to a non-axisymmetrical, off-design aerodynamic profile. However, the shell's shape and the vehicle's attitude remained stable. A nutation motion with the amplitude decaying through descent has been observed.

It is still required to experiment in the upper atmosphere at higher speed and dynamic pressure, in order to adequately understand the deployment and flight dynamic behaviour. The present study suggests that a suborbital/orbital experiment is possible with test vehicle constructed from existing high-temperature ceramic fibres that are flight-proven in NASA's inflatable aeroshell tests. Further study also needs to qualify the material for the thermal and mechanical load during a re-entry with rapid deformation.

Reference

[1] R. D. Braun, R. M. Manning, Mars exploration entry, descent, and landing challenges, Journal of Spacecraft and Rockets 44 (2) (2007) 310–323.

[2] B. Steinfeldt, J. Theisinger, A. Korzun, I. Clark, M. Grant, R. Braun, High mass Mars entry, descent, and landing architecture assessment, in: AIAA SPACE 2009 Conference & Exposition, AIAA paper 2009-6684.

[3] B. G. Drake, S. J. Hoffman, D. W. Beaty, Human exploration of Mars, design reference architecture 5.0, in: Aerospace Conference, IEEE, 2010, pp. 1–24.

[4] J. Cruz, J. Lingard, Aerodynamic decelerators for planetary exploration: past, present, and future, in: AIAA Guidance, Navigation, and Control Conference and Exhibit, AIAA paper 2006-6792.

[5] S. Dutta, B. Smith, D. Prabhu, E. Venkatapathy, Mission sizing and trade studies for low ballistic coefficient entry systems to Venus, in: Aerospace Conference, IEEE, 2012, pp. 1–14.

[6] A. Cassell, P. Wercinski, B. Smith, B. Yount, O. Nishioka, C. Kruger, ADEPT sounding rocket one flight test overview, in: AIAA Aviation 2019 Forum, AIAA paper 2019-2896.

[7] V. Carandente, R. Savino, New concepts of deployable de-orbit and re-entry systems for Cubesat miniaturized satellites, Recent Patents on Engineering 8 (1) (2014) 2–12.

[8] J. Andrews, K. Watry, K. Brown, Nanosat deorbit and recovery system to enable new missions, SSC11-X-3, presented at the 25th AIAA/USU Conference on Small Satellites, Logan, Utah, USA, 8-12 August, 2011.

[9] B. Smith, A. Cassell, C. Kruger, E. Venkatapathy, C. Kazemba, K. Simonis, Nano-ADEPT: An entry system for secondary payloads, in: Aerospace Conference, IEEE, 2015, pp. 1–11.

[10] M. Wiegand, H. Konigsmann, A small re-entry capsule-BREM-SAT 2, in: 10th AIAA/USU Small Satellite Conference, Logan, UT, Volume 1, 1996.

[11] B. P. Smith, C. L. Tanner, M. Mahzari, I. G. Clark, R. D. Braun, F. M. Cheatwood, A historical review of inflatable aerodynamic decelerator technology development, in: Aerospace Conference, IEEE, 2010, pp. 1–18.

[12] I. G. Clark, A. L. Hutchings, C. L. Tanner, R. D. Braun, Supersonic inflatable aerodynamic decelerators for use on future robotic missions to Mars, in: Aerospace Conference, IEEE, 2008, pp. 1–17.

[13] H. Bohon, M. Mik, Development status of attached inflatable decelerators, Journal of Spacecraft and Rockets 6 (6) (1969) 654–660.

[14] C. Tanner, J. Cruz, R. Braun, Structural verification and modeling of a tension cone inflatable aerodynamic decelerator, in: 51st AIAA/ASME/ASCE/AHS/ASC Structures, Structural Dynamics, and Materials Conference 18th AIAA/ASME/AHS Adaptive Structures Conference, AIAA paper 2010-2830.

[15] A. Mastropietro, J. Kempenaar, M. Redmond, M. Pauken, W. Ancarrow, First test flight thermal performance of the low density supersonic decelerator (LDSD) supersonic flight dynamics test (SFDT) vehicle, in: 45th International Conference on Environmental Systems, 2015.

[16] D. Litton, D. Bose, F. Cheatwood, S. Hughes, H. Wright, M. Lindell, S. Derry, A. Olds, Inflatable re-entry vehicle experiment IRVE-4 overview, in: 21st AIAA Aerodynamic Decelerator Systems Technology Conference and Seminar, AIAA paper 2011-2580.

[17] D. Wilde, S. Walther, K. Pitchadze, S. Alexsaschkin, D. Vennemann, L. Marraffa, Flight test and ISS application of the inflatable reentry and descent technology (IRDT), Acta Astronautica 51 (1-9) (2002) 83–88.

[18] Y. Takahashi, T. Ohashi, N. Oshima, Y. Nagata, K. Yamada, Aerodynamic instability of an inflatable aeroshell in suborbital re-entry, Physics of Fluids 32 (7) (2020) 075114.

[19] Y. Takahashi, T. Koike, N. Oshima, K. Yamada, Aerothermodynamic analysis for deformed membrane of inflatable aeroshell in orbital reentry mission, Aerospace Science and Technology 92 (2019) 858–868.

[20] C. Dek, J.-L. Overkamp, A. Toeter, T. Hoppenbrouwer, J. Slimmens, J. van Zijl, P. A. Rossi, R. Machado, S. Hereijgers, V. Kilic, et al., A recovery system for the key components of the first stage of a heavy launch vehicle, Aerospace Science and Technology 100 (2020) 105778.

[21] J. Guo, G. Lin, J. Zhang, X. Bu, H. Li, Hypersonic aerodynamics of a deformed aeroshell in continuum and near-continuum regimes, Aerospace Science and Technology 93 (2019) 105296.

[22] Y. Takahashi, D. Ha, N. Oshima, K. Yamada, T. Abe, K. Suzuki, Aerodecelerator performance of flare-type membrane inflatable vehicle in suborbital reentry, Journal of Spacecraft and Rockets 54 (5) (2017) 993–1004.

[23] J. F. Martiarena, V. N. Mora, J. Piechocki, Experimental study of the effect of blade curvature and aspect ratio on the performance of a rotary-wing decelerator, Aerospace Science and Technology 43 (2015) 471–477.

[24] D. L. Akin, The parashield entry vehicle concept-basic theory and flight test development, in: 4th AIAA/USU Small Satellite Conference, Logan, UT, Aug. 27-30, 1990, Proceedings. (A91-27376 10-18), Vol. 1, 1990.

[25] K. Kwok, S. Pellegrino, M. Quadrelli, G. Davis, D. Boussalis, Structural and control concepts for variable geometry planetary entry systems, in: 50th AIAA/ASME/ASCE/AHS/ASC Structures, Structural Dynamics, and Materials, AIAA paper 2009-2100.

[26] E. Venkatapathy, K. Hamm, I. Fernandez, J. Arnold, D. Kinney, B. Laub, A. Makino, M. McGuire, K. Peterson, D. Prabhu, et al., Adaptive deployable entry and placement technology (ADEPT): a feasibility study for human missions to Mars, in: 21st AIAA Aerodynamic Decelerator Systems Technology Conference and Seminar, AIAA paper 2011-2608.

[27] E. Fantino, M. Grassi, P. Pasolini, F. Causa, C. Molfese, R. Aurigemma, N. Cimminiello, D. de la Torre, P. Dell'Aversana, F. Esposito, et al., The small Mars system, Acta Astronautica 137 (2017) 168–181.

[28] G. Zuppardi, R. Savino, G. Mongelluzzo, Aero-thermo-dynamic analysis of a low ballistic coefficient deployable capsule in Earth re-entry, Acta Astronautica 127 (2016) 593–602.

[29] V. Carandente, R. Savino, V. DOriano, R. Fortezza, A study on Earth re-entry capsules with deployable aerobrakes for recoverable microgravity experiments, Microgravity Science and Technology 27 (3) (2015) 181–191.

[30] S. Mungiguerra, G. Zuppardi, R. Savino, Rarefied aerodynamics of a deployable re-entry capsule, Aerospace Science and Technology 69 (2017) 395–403.

[31] D. O'Driscoll, P. J. Bruce, M. J. Santer, Origami-based TPS folding concept for deployable mars entry vehicles, in: AIAA Scitech 2020 Forum, AIAA paper 2020-1897.

[32] R. Wu, P. C. Roberts, C. Soutis, C. Diver, Flexible heat shields deployed by centrifugal force, Acta Astronautica 152 (2018) 78–87.

[33] R. Wu, P. C. Roberts, C. Soutis, C. Diver, Downrange manoeuvre and oscillation suppression of a self-regulating centrifugally deployed flexible heat shield using a controlled reaction wheel, Acta Astronautica 161 (2019) 415–424.

[34] S. Hughes, J. Ware, J. Del Corso, R. Lugo, Deployable aeroshell flexible thermal protection system testing, in: 20th AIAA Aerodynamic Decelerator Systems Technology Conference and Seminar, AIAA paper 2009-2926.

[35] H. Wright, A. Cutright, J. Corliss, W. Bruce, D. Trombetta, A. Mazaheri, M. Coleman, A. Olds, S. Hancock, HEART flight test overview, in: 9th International Planetary Probe Workshop, Toulouse, France, 2012.

[36] K. Szltton, R. A. Graues Jr, A general stagnation-point convective-heating equation for arbitrary gas mixtures, Tech. rep., NASA TR-R-376 (1971).

[37] P. Gallais, Atmospheric re-entry vehicle mechanics, Springer Science & Business Media, 2007.

[38] A. K. Chinnappan, G. Malaikannan, R. Kumar, Insights into flow and heat transfer aspects of hypersonic rarefied flow over a blunt body with aerospike using direct simulation monte-carlo approach, Aerospace Science and Technology 66 (2017) 119–128.

[39] H. Allen, A. Eggers Jr, A study of the motion and aerodynamic heating of missiles entering the atmosphere at high supersonic speeds, Tech. rep., NACA RM-A23D28 (1953).

[40] A. D. Ketsdever, M. M. Micci, Micropropulsion for small spacecraft, American Institute of Aeronautics and Astronautics, 2000.

[41] G. P. Sutton, O. Biblarz, Rocket propulsion elements, John Wiley & Sons, 2016.

[42] D. W. Way, R. W. Powell, A. Chen, A. D. Steltzner, A. M. San Martin, P. D. Burkhart, G. F. Mendeck, Mars science laboratory: Entry, descent, and landing system performance, in: Aerospace Conference, IEEE, 2007, pp. 1–19.

[43] R. M. Crow, M. M. Dewar, Comparison of seam types, Tech. rep., Defence Research Establishment Ottawa (Ontario) (1983).

[44] P. Wercinski, Adaptable deployable entry & placement technology (ADEPT) for cubesat delivery to Mars surface, Tech. rep., NASA ARC-E-DAA-TN19332 (2014).